Irradiance-Adaptive PV Module Integrated Converter for High Efficiency and Power Quality in Standalone and DC Microgrid Applications

Moustafa Adly, *Student Member, IEEE*, and Kai Strunz

***Abstract*—The strive for efficient and cost-effective photovoltaic (PV) systems motivated the power electronic design developed here. The work resulted in a dc–dc converter for module integration and distributed maximum power point tracking (MPPT) with a novel adaptive control scheme. The latter is essential for the combined features of high energy efficiency and high power quality over a wide range of operating conditions. The switching frequency is optimally modulated as a function of solar irradiance for power conversion efficiency maximization. With the rise of irradiance, the frequency is reduced to reach the conversion efficiency target. A search algorithm is developed to determine the optimal switching frequency step. Reducing the switching frequency may, however, compromise MPPT efficiency. Furthermore, it leads to increased ripple content. Therefore, to achieve a uniform high power quality under all conditions, interleaved converter cells are adaptively activated. The overall cost is kept low by selecting components that allow for implementing the functions at low cost. Simulation results show the high value of the module integrated converter for dc standalone and microgrid applications. A 400-W prototype was implemented at 0.14 Euro/W. Testing showed efficiencies above 95 %, taking into account all losses from power conversion, MPPT, and measurement and control circuitry.**

***Index Terms*—Boost converter, distributed maximum power point tracking (DMPPT), microgrid, module integrated converter (MIC), photovoltaics (PV), power optimizer, power quality, solar irradiance, switching frequency modulation (SFM).**

I. Introduction

SOLAR energy conversion through photovoltaics (PV) is a rapidly growing source of green power supply [1]. Improving the efficiency of PV systems is widely seen as important in supporting this trend [2], [3]. This concerns not only the improvement of the PV cells but of the power electronic circuits and controls connected to them as well.

Manuscript received November 28, 2016; revised May 16, 2017; accepted June 12, 2017. Date of publication August 4, 2017; date of current version November 16, 2017. This work was supported by the German academic exchange service DAAD. *(Corresponding author: Moustafa Adly.)*

The authors are with the Chair of Sustainable Electric Networks and Sources of Energy, Technische Universität Berlin, D-10587 Berlin, Germany (e-mail: m.adly@mailbox.tu-berlin.de; kai.strunz@tu-berlin.de).

Color versions of one or more of the figures in this paper are available online at http://ieeexplore.ieee.org.

Digital Object Identifier 10.1109/TIE.2017.2723860

Beyond the PV cells, the overall PV system efficiency is greatly affected by three factors. First, it is affected by the granularity level of distributed maximum power point tracking (DMPPT) [2], [4]–[6]. Second, it is influenced by the accuracy and speed of the utilized maximum power point tracking (MPPT) algorithm [7]. Third, the power conversion efficiency of the employed converter topology plays a key role [3], [8], [9]. Regarding the first factor, module integrated converters (MICs) or power optimizers representing module-level DMPPT highly improve PV power harvesting efficiency [3], [9]–[11]. With respect to the second factor, recent research has considered employing various converter topologies and novel MPPT algorithms within MICs for PV system efficiency maximization [8], [10]. Buck and boost as basic nonisolated power converters are widely employed in MICs [3], [9]–[11]. In this context, the power conversion efficiency of the MIC topology as a third factor is highly impacted by the utilized modulation scheme [9], [12]–[14].

Switching frequency modulation (SFM) is a form of pulse width modulation (PWM) utilizing multiple switching frequencies in controlling dc–dc converters [12], [15]–[17]. The SFM has been employed for the following applications. It has contributed to the reduction of electromagnetic interference (EMI) emission by power spectrum spreading [18]–[20]. In [21], SFM was utilized for power line communication in dc microgrids, where all power converters share a common dc bus. Minimizing output current total harmonic distortion in current source inverters through an SFM scheme was introduced in [22]. In addition, SFM has improved the robustness to the variations of resonance parameters and input voltages in current source parallel resonant converters [23]. Also, SFM has been used for load-dependent optimization of power conversion efficiency at any conduction mode [15]–[17].

The successful application of SFM in load-dependent optimization suggests that it may also be an attractive candidate when generation heavily varies. Such a situation is encountered in the solar power harvesting of MICs. This observation has motivated the work for this paper to investigate the contribution of the SFM to further improve the PV system efficiency beyond the three factors discussed above.

In the scientific literature, only fixed switching frequencies have been reported in the control of the MICs [3], [5]. Values of 20, 40, 50, 75, 85, 100, and 250 of the switching frequency in kilohertz were used [3], [5], [6], [10]. The fixed switching

frequency was selected to maintain the continuous conduction mode (CCM) of the MIC at all analyzed irradiance levels. Thus, a continuous power flow was attained, and the harvested power from the PV source was increased [14]. However, the selection of a fixed switching frequency involves a tradeoff. At high irradiance, when the PV current is high, a lower switching frequency would be possible. A higher switching frequency reduces the power conversion efficiency due to switching losses. It is the first contribution of this paper to design an irradiance-adapted SFM scheme for MICs to optimize the MIC efficiency at all irradiance levels. So, the overall energy harvested through the PV system is improved. A novel stepwise procedure with an integrated automated search algorithm to determine the number and values of the optimal switching frequencies of the SFM based on the irradiance is developed.

Another desirable feature is uniform power quality. Attaining a uniform power quality is challenging when an SFM modulates the switching frequency. As a potential solution, interleaved converters show high ability of modifying the output ripple [24], [25]. Moreover, they can improve efficiency and reduce EMI [24]–[27]. Tackling the nonuniform ripple content resulting from SFM has not been addressed so far in the scientific literature. As a complementary contribution to the irradiance-adaptive SFM, the appropriate number of cells for an adaptive converter topology and the corresponding activation times in correlation to the SFM scheme are developed. This has the outcome of the reduced ripple content and EMI emission. The above claims on efficiency, output ripple, and EMI are substantiated by physical implementation and testing of the MIC. The performed experiments covered standalone and dc microgrid applications.

Following this introduction, the adaptive SFM scheme and MIC topology for PV applications is presented in Section II. Furthermore, the combination with a fast reacting MPPT is illustrated. In Section III, issues of dc microgrid integration are addressed. Simulation results and experimental validation are presented in Sections IV and V, respectively. Conclusions are drawn in Section VI. In addition, the realization of the MIC at a low cost is elaborated upon in the Appendixes.

II. PV-Adapted Switching Frequency Modulation

Employing optimal SFM in PV systems is introduced in three main parts: the irradiance-adaptive SFM, the optimization of the SFM scheme and MIC topology, and the MPPT algorithm.

A. Irradiance-Adaptive SFM

The PV current increases in strength with the solar irradiance. At high irradiance, the PV-fed MIC can operate in the CCM for a wide load range. Low switching frequencies in that case can contribute to a high efficiency without altering the converter mode of operation to the discontinuous conduction mode (DCM). At low irradiance and due to the low supply current, the converter may move to the DCM. The instantaneous power drawn from input sources is zero at the moment when the inductor current is zero in the DCM [14]. Increasing the switching frequency can keep operation in the CCM. Therefore, the switching frequency f_s is proposed to be adaptively

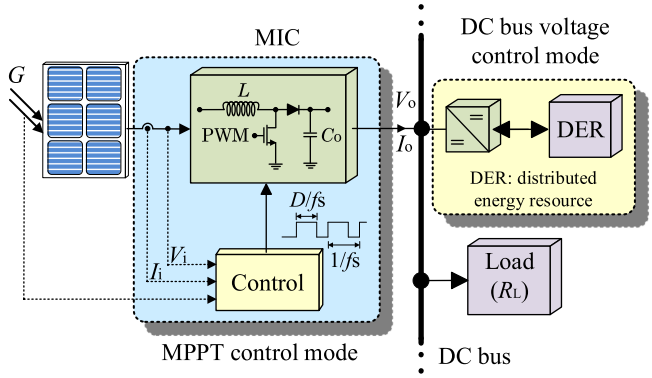

Fig. 1. PV module integrated converter in dc microgrid application.

controlled with the solar irradiance G as an input as

$$f_s = \begin{cases} f_{s0} = f_{s\max}, & G_0 \leqslant G < G_1 \\ f_{si} = f_{s(i-1)} - \Delta f_{si}, & 1 \leqslant i \leqslant n, G_i \leqslant G < G_{i+1} \end{cases} \tag{1}$$

where i is the counter of discrete switching frequency f_{si}, $f_{s\max}$ is the maximum switching frequency representing f_{si} for $i = 0$, Δf_{si} denotes the frequency variation step i, G_0 and G_{n+1} are the minimum and maximum irradiances considered, respectively, and G_i for $i = 1, 2, ..., n$ are the intermediate irradiance thresholds. For constant Δf_s, (1) reduces to

$$f_{si} = f_{s\max} - i \cdot \Delta f_s, \qquad 0 \leqslant i \leqslant n. \tag{2}$$

To identify the minimum switching frequency for CCM operation of the MIC, (16) of Appendix A relating f_s, PWM duty ratio D, and PV module steady-state average voltage V_i and current I_i is rearranged as follows:

$$f_s \geq \frac{D \cdot V_i}{2 \cdot I_i \cdot L}. \tag{3}$$

The duty ratio D for a boost converter of efficiency η is approximated by [28]

$$D = 1 - \frac{\eta \cdot V_i}{V_o} \tag{4}$$

where V_o is the steady-state average output voltage of the MIC.

In Fig. 1, the MIC is shown feeding a dc bus of a microgrid. In such cases, V_o is the dc-bus voltage. Insertion of (4) into (3) yields

$$f_s \geq \frac{V_i}{2 \cdot I_i \cdot L} \cdot \left(1 - \frac{\eta \cdot V_i}{V_o}\right). \tag{5}$$

For the analysis of standalone applications, the MIC is assumed to directly supply a load with no other distributed energy resource (DER) control. So, for a pure resistive load R_L, V_o is given by

$$V_o = \sqrt{\eta \cdot V_i \cdot I_i \cdot R_L}. \tag{6}$$

Through (5) and (6), the minimum boundary of the switching frequency for CCM operation in standalone application is estimated as follows:

$$f_s \geq \frac{V_i}{2 \cdot I_i \cdot L} \cdot \left(1 - \sqrt{\frac{\eta \cdot V_i}{I_i \cdot R_L}}\right). \tag{7}$$

B. Optimization of SFM Scheme and MIC Topology

1) SFM Scheme Parameters: The SFM scheme parameters cover the following quantities: the minimum switching frequency $f_{\mathrm{s\,min}}$, the maximum switching frequency $f_{\mathrm{s\,max}}$, the frequency steps Δf_{si}, and the irradiance thresholds G_i. The optimal value of the frequency step and MIC topology for high efficiency and power quality are determined. More focus is dedicated to the boost converter as a MIC topology for reasons stated in Section III. The SFM scheme for the buck converter case is described in Appendix B. The derivation of the parameters in the following steps applies to the boost converter.

Step 1: The minimum switching frequency $f_{\mathrm{s\,min}}$ calculated here corresponds to the highest irradiance in (1). It is determined based on two targets that are related to energy efficiency and output voltage ripple. High switching frequencies reduce the peak-to-peak output voltage ripple ΔV_{opp}:

$$\Delta V_{\mathrm{opp}} = \frac{I_{\mathrm{o}} \cdot D}{C_{\mathrm{o}} \cdot f_{\mathrm{s}}} \tag{8}$$

where C_{o} is the capacitance of the MIC output capacitor, and I_{o} is the steady-state average output current of the MIC. However, higher switching frequencies reduce the MIC efficiency due to switching losses. The minimum employed switching frequency must meanwhile satisfy the condition of the CCM. Therefore, the switching frequency boundary for CCM operation at different irradiances is determined first. The values of V_{i} and I_{i} of the PV module at maximum power point (MPP) under different irradiances G are inserted into (5) and (7). A target efficiency η and the maximum load resistance R_{L} in the case of standalone applications are used to get the CCM switching frequency boundary of the considered boost converter and the analyzed PV module. The trajectory obtained is depicted in Fig. 2(a) representing the worst case across all practical operating conditions. Similarly, for various dc-bus voltages V_{o}, the trajectory obtained for the microgrid case is depicted in Fig. 2(b).

A safety margin for robustness toward uncertainty in the parameters was included in the boundary. At the highest irradiance shown in Fig. 2, the minimum switching frequency for CCM operation is $f_{\mathrm{s\,min\,CCM}}$. A final value of $f_{\mathrm{s\,min}}$ is obtained by also including a constraint for a desired voltage ripple in addition to the CCM constraint. The final value for f_{smin} cannot be lower but may be higher than $f_{\mathrm{s\,min\,CCM}}$.

Step 2: The maximum switching frequency $f_{\mathrm{s\,max}}$ is dependent on the boundary of operating the converter in CCM at the lowest irradiance. From Fig. 2, the lower limit of the maximum switching frequency at the lowest irradiance threshold G_0 can be determined. For minimal switching losses, the value of f_{s} at G_0 in Fig. 2 is confirmed as $f_{\mathrm{s\,max}}$.

The selection of a low $f_{\mathrm{s\,max}}$ also keeps the range $(f_{\mathrm{s\,max}} - f_{\mathrm{s\,min}})$ rather tight. As found in [17], such a tight range can reduce detrimental effects on the phase margin and the crossover frequency of the converter control.

Step 3: In this step, the switching frequency step $\Delta f_{\mathrm{s\,min}}$ that corresponds to the minimum detectable irradiance change ΔG_{min} is computed. On the one hand, large values of Δf_{s} can reduce f_{s} faster and contribute to reducing the converter power loss. However, the CCM operation condition may be violated. On the other hand, when selecting a certain Δf_{s}, then there is a

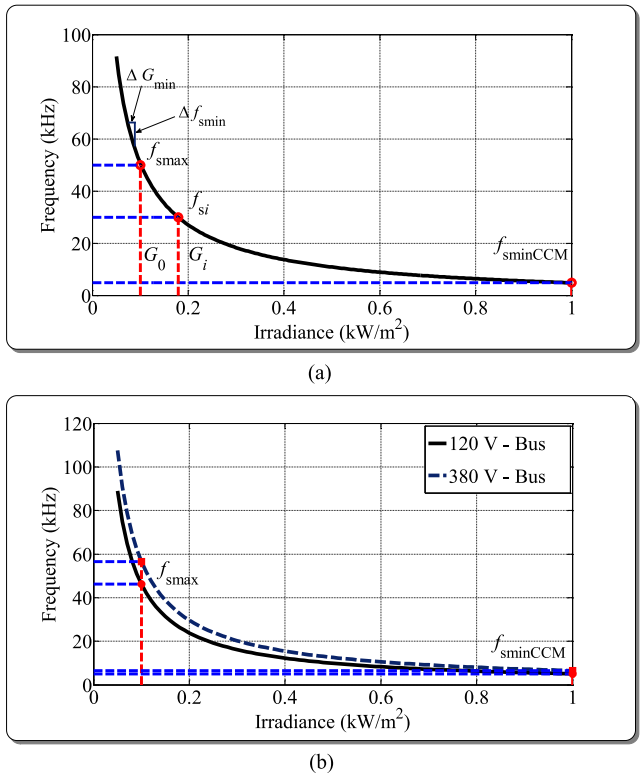

Fig. 2. Trajectory of the switching frequency boundary for operating boost converter in the CCM at different irradiance levels for (a) the standalone case using (7) and (b) the microgrid case using (5).

corresponding ΔG when following the trajectory of Fig. 2. Thus, a lower limit $\Delta f_{\mathrm{s\,min}}$ can be set for satisfying the constraint of ΔG_{min} while following the trajectory.

In what follows, an expression of Δf_{s} in terms of ΔG is derived, and then, $\Delta f_{\mathrm{s\,min}}$ is estimated. As the solar irradiance G has a strong impact on the converter input current, the rate of change of the switching frequency in (3) with respect to the converter input current is of interest. The change in V_{i} with a small variation of I_{i} is assumed to be negligible around the MPP. It will also be assumed that the change in the duty ratio D of the digital controller due to a small change in I_{i} is less than its minimum step ΔD, and therefore, D is considered unchanged. So, differentiating f_{s} with respect to I_{i} yields

$$\frac{df_{\mathrm{s}}}{dI_{\mathrm{i}}} \geq \frac{-D \cdot V_{\mathrm{i}}}{2 \cdot I_{\mathrm{i}}^2 \cdot L}. \tag{9}$$

According to (2), a $\Delta f_{\mathrm{s}} > 0$ reduces f_{s}. Approximating in (9) $-\Delta f_{\mathrm{s}} = df_{\mathrm{s}}$ and $\Delta I_{\mathrm{i}} = dI_{\mathrm{i}}$ gives

$$\Delta f_{\mathrm{s}} \leq \frac{D \cdot V_{\mathrm{i}}}{2 \cdot I_{\mathrm{i}}^2 \cdot L} \cdot \Delta I_{\mathrm{i}}. \tag{10}$$

Then, from the approximate linear relation between the MPP current and the solar irradiance, $\Delta f_{\mathrm{s\,min}}$ is obtained using

$$\Delta f_{\mathrm{s\,min}} = \frac{D \cdot V_{\mathrm{i}} \cdot K}{2 \cdot I_{\mathrm{i}}^2 \cdot L} \cdot \Delta G_{\mathrm{min}} \tag{11}$$

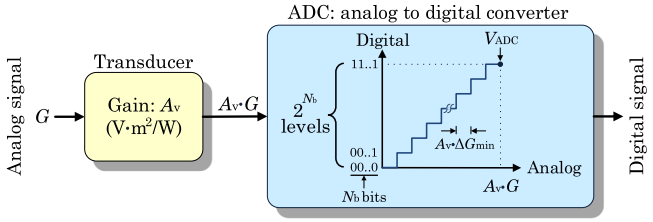

Fig. 3. Discretization of the irradiance for the SFM scheme control.

where K is approximated as the ratio of the MPP current change to the irradiance change under standard test conditions (STCs):

$$K = \frac{\Delta I_{\mathrm{i}}}{\Delta G}. \tag{12}$$

The minimum change in G that can be sensed by the analog-to-digital converter (ADC) of the control chip ΔG_{min} is

$$\Delta G_{\mathrm{min}} = \frac{V_{\mathrm{ADC}}}{2^{N_{\mathrm{b}}} \cdot A_{\mathrm{v}}} \tag{13}$$

where V_{ADC} is the maximum voltage that can be sensed by the ADC, N_{b} is the number of ADC bits, and A_{v} is the employed irradiance sensing gain. The discretization of the solar irradiance for further processing by the digital control is shown in Fig. 3. Since the slope of the curve in Fig. 2 decreases with the increase of G, the maximum value of $\Delta f_{\mathrm{s\,min}}$ is, therefore, obtained at the lowest irradiance.

It is important to note that Δf_{s} is selected first, and only then ΔG is determined. When Δf_{s} is set higher than $\Delta f_{\mathrm{s\,min}}$, then ΔG is also larger than ΔG_{min}, giving a feasible practical implementation.

Step 4: The employed switching frequency step Δf_{s} is determined in this step. A fixed-frequency step is assumed as in (2). Therefore, the frequency step Δf_{s} and the number of employed frequencies n+1 are related by

$$\Delta f_{\mathrm{s}} = \frac{f_{\mathrm{s\,max}} - f_{\mathrm{s\,min}}}{n}. \tag{14}$$

The switching frequency step must be greater than $\Delta f_{\mathrm{s\,min}}$ in (11). Since a fixed-frequency step is utilized, $\Delta f_{\mathrm{s\,min}}$ is calculated at the lowest irradiance where it is at its maximum. Meanwhile, an integer value of Δf_{s} is used for practical implementation.

A searching algorithm for Δf_{s} under the mentioned constraints is then performed. The algorithm increments the integer n and determines Δf_{s} from (14). Then, it computes the employed switching frequencies $f_{\mathrm{s}i}$ from (2) and their corresponding irradiance thresholds G_i, as in Fig. 2. Hereafter, the algorithm calculates the corresponding MIC power loss for the analyzed irradiance ranges using (18)–(24) of Appendix A. The algorithm stops when Δf_{s} becomes less than $\Delta f_{\mathrm{s\,min}}$ or when the further average reduction of the MIC power loss with increased n is less than a certain practical limit. The obtained Δf_{s} and set of G_i thresholds are retained.

Step 5: A hysteresis of the irradiance thresholds is introduced in this step. In order to avoid an unwanted bouncing or frequent variation of the switching frequency due to inaccuracies, for example as a result of flying objects or sensor faults, a hysteresis is proposed to complement (1) and (2). For the case of four switching frequencies, Fig. 4 shows the proposed variation of the switching frequency with the solar irradiance. The deadbands are designed not to exceed the CCM boundary, as in Fig. 4.

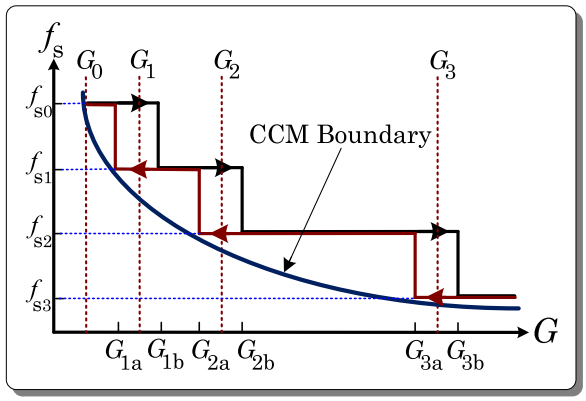

Fig. 4. Irradiance-based hysteresis control of switching frequency.

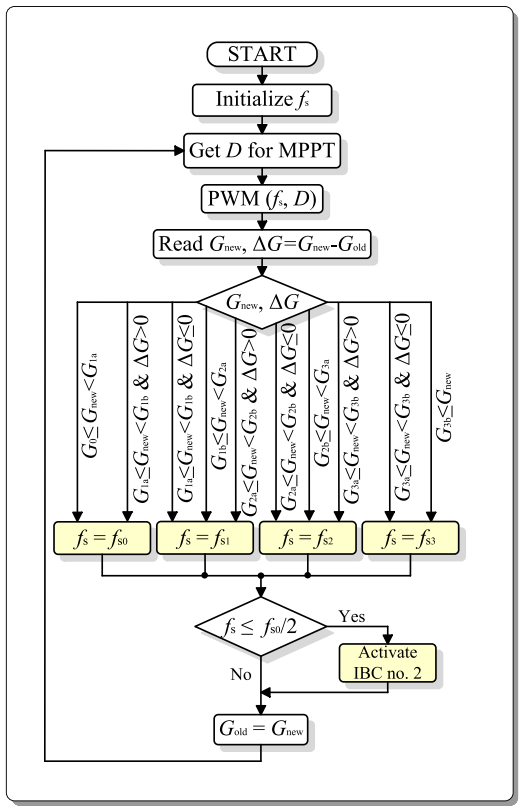

Fig. 5. Flowchart of the adaptive MIC control scheme.

The SFM control algorithm is presented in Fig. 5 for four switching frequencies. The algorithm starts with the highest switching frequency, for operation in the CCM. The duty ratio D is obtained from the MPPT algorithm, and the PWM is updated. Based on the new irradiance measurement G_{new} and the irradiance change $\Delta G = G_{\mathrm{new}} - G_{\mathrm{old}}$, the switching frequency is then updated, too.

2) MIC Topology: Combining an adaptive MIC topology with the optimized SFM scheme further contributes to the

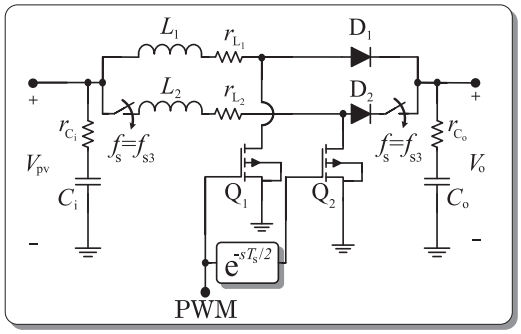

Fig. 6. Converter topology of the boost converter with an interleaved cell activated at low switching frequency f_{s3}.

design objective of maintaining high-level power quality. Without an adaptive topology, the variation of the ripple results in a nonuniform power quality level over the range of f_s employed. For an almost uniform output ripple content and less EMI emission at all frequencies, interleaved converter cells are activated as a function of the decreasing switching frequency. Also, for the MPPT, it is advantageous that the input current ripple drawn from the PV module is also reduced [10]. The proposed number of interleaved cells is the integer truncation of the ratio $f_{s\max}/f_{s\min}$. Based on the used switching frequency, the adaptive control decides on the number of interleaved boost converter cells (IBCs) to be activated. The number of active cells is set to be equal to j for switching frequencies less than or equal to $f_{s\max}/j$.

The converter topology of the prototype with two interleaved cells is shown in Fig. 6. The second IBC is activated whenever f_s is less than $f_{s\max}/2$, as also shown in Fig. 5, where $f_{s\max} = f_{s0}$. For the given four discrete switching frequencies of the SFM, this is the case when $f_s = f_{s3}$. Thanks to the activation, the EMI gets less and power quality remains high for a wide range of sensitive loads [29], [30]. At low irradiance, the higher switching frequency improves the power quality, at the expense of higher switching losses. Activating the IBC in this case would lead to a relatively low improvement of an already good power quality at extra losses. So, the IBC is only activated at the low switching frequency.

It is to be noted that the loss minimization performed in Step 4 of the SFM design is consistent with the adaptive MIC topology. At low irradiance, switching losses dominate conduction losses and vice versa, as can be concluded from (18)–(24) of Appendix A. At high irradiance, when the interleaved cell is activated, the overall losses are reduced because the conduction loss reduction exceeds the switching loss increase. Thus, while improving power quality, power conversion efficiency objectives are also fully supported by the adaptive MIC topology.

C. Maximum Power Point Tracking

The perturb and observe (P&O) algorithm with the minimum perturbation step size for accurate DMPPT is employed. The MPP voltage V_{MPP} theoretically lies between 75 % and 90 % of the open-circuit voltage V_{oc}. Thus, the P&O algorithm is designed to start with an initial duty ratio corresponding to 75 % of V_{oc} [31] to reduce the tracking time. The module voltage and current are sensed at each step after settling, and a new D is determined.

III. DC Microgrid Integration

The adaptively controlled MIC is proposed for module-level integration into the dc microgrid, as shown in Fig. 1. The input voltage of the MIC is adjusted for MPPT, and the output voltage is defined by the dc-bus voltage control units. Therefore, each PV-MIC combination acts as a current source.

Thus, the MIC is required to have input and output ratings suitable for the common PV modules and the bus voltage of the low-voltage dc microgrid, respectively. An MIC output voltage with a low ripple is, meanwhile, very desirable.

As popular voltages for dc microgrids, levels reported include 120, 170, 230, 340, and 380 V [32], [33]. Higher dc-bus voltages necessitate higher switching frequencies for maintaining CCM operation, as concluded from Fig. 2(b). Furthermore, to step up the commonly low PV module voltages, boost converter topologies are needed. The freewheeling diode of the boost converter can stop any reverse current from the dc bus and so protect the PV modules. Nonetheless, there are also situations where buck converter topologies are appropriate. Therefore, selected information for the buck case is provided in Appendix B.

In the case of a boost converter, the appropriate MIC input voltage range for dc microgrid integration is obtained from (4) by

$$\frac{1-D_{\max}}{\eta}\cdot V_o < V_i < \frac{1-D_{\min}}{\eta}\cdot V_o \qquad (15)$$

where $D_{\min}$ and $D_{\max}$ are the minimum and maximum duty ratios, respectively. PV modules with MPP voltages violating the lower limit of (15) are integrated with converters having higher voltage gains [3]. PV modules violating the upper limit of (15) would be integrated using buck converters.

IV. Analysis by Simulation

In this section, the adaptive topology and optimal SFM scheme are analyzed by simulation. Parameters of the SFM scheme are determined in a first step. Then, simulation cases under variable irradiance patterns are described for standalone and dc microgrid cases. MATLAB/SIMULINK was used to simulate the PV-MIC system and the proposed control scheme. The converter circuit components were designed to fulfill the objectives of the MIC with input capacitance C_i of 220 μF, output capacitance C_o of 2200 μF, and inductances $L_{1,2}$ of 0.5 mH. The simulated PV module has a V_{oc} of 44.8 V, V_{MPP} of 36.5 V, short-circuit current I_{sc} of 5.5 A, and MPP current I_{MPP} of 5.1 A under standard test conditions (STCs). The parameters of the MPPT control algorithm based on the utilized hardware are minimum duty ratio $D_{\min}$ of 10 %, maximum duty ratio $D_{\max}$ of 90 %, duty ratio step ΔD of 0.4 %, and 10 ADC bits as N_b.

A. SFM Scheme Parameters

The procedure of Section II-B1 was followed for the purpose of determining the SFM scheme parameters. In Step 1, an efficiency higher than 97 % and an output voltage ripple of 0.5 % were targeted. The value found for $f_{s\min}$ was determined to be

20 kHz, satisfying the CCM condition represented by $f_{s\min CCM}$ of Fig. 2.

In Step 2, the maximum switching frequency $f_{s\max}$ was determined. The lowest analyzed irradiance G_0 was proposed to be 0.1 kW/m^2. From Fig. 2, a maximum switching frequency $f_{s\max}$ of about 50 kHz keeps the converter in the CCM for an analyzed load range from 0 to 3 kΩ.

For step 3, $\Delta G_{\min}$ was calculated using (13) with V_{ADC} of 5 V and A_v of 0.005 V · m^2/W. The parameter K is equal to 0.0051 A · m^2/W. The lowest irradiance G_0 was used to get $\Delta f_{s\min}$ from (11). The values of V_i, I_i, and D for the calculation of $\Delta f_{s\min}$ were 26.7 V, 0.5 A, and 0.8, respectively. The computation resulted in a value of 429 Hz for $\Delta f_{s\min}$ corresponding to a minimum detectable irradiance change $\Delta G_{\min}$ of 0.98 W/m^2.

For Step 4, an integer optimal value of 10 kHz for Δf_s was the outcome of the searching algorithm, and the number of frequencies was four. For values of n higher than 4, the reduction of the MIC power loss was less than a proposed practical limit of 0.2 %. The switching frequencies are then 50, 40, 30, and 20 kHz. Based on Fig. 2, the corresponding irradiance thresholds in kW/m^2 were set to 0.1, 0.15, 0.2, and 0.35.

In Step 5, a hysteresis deadband of 0.04 kW/m^2 was selected. So, G_{1a}, G_{1b}, G_{2a}, G_{2b}, G_{3a}, and G_{3b} as in Fig. 4 were assigned the following values in kW/m^2: 0.13, 0.17, 0.18, 0.22, 0.33, and 0.37.

The truncated integer of the ratio $f_{s\max}/f_{s\min}$ is equal to 2. Therefore, two boost converter cells were employed in the MIC, as shown in Fig. 6. The second IBC is activated at switching frequencies less than $f_{s\max}/2$, therefore, only at f_{s3}.

B. Variable Irradiance Cases

In this subsection, the performance of the PV-MIC system for two solar irradiance time series following stepwise changing and continuously changing patterns is discussed. First, the performance under a stepwise changing irradiance with four levels 0.1, 0.175, 0.3, and 1 kW/m^2 was analyzed. The solar irradiance, the switching frequency, and the output power are depicted in Fig. 7(a). The MIC control was able to vary the switching frequency adaptively with the solar irradiance according to the SFM scheme. Meanwhile, the maximum PV power was efficiently tracked. The converter was in the CCM in the four cases. The interleaved converter cell is only activated at the highest irradiance level at a switching frequency of 20 kHz. This, in turn, reduces the output voltage ripple from 1.30 % to 0.59 %. It is in the same range as for the other irradiance levels.

The effect of continuously changing irradiance patterns on both the switching frequency and the output power is presented in Fig. 7(b). The hysteresis involved in the SFM of Fig. 4 can be observed as follows. When the irradiance rises and crosses 0.17 kW/m^2 after 10.8 s into the simulation, the switching frequency is reduced from 50 to 40 kHz. In the opposite direction from 40 to 50 kHz, this happens at 0.13 kW/m^2 after 49.7 s and falling irradiance. Similar outcomes are observed for the transitions from 40 to 30 kHz and from 30 to 20 kHz.

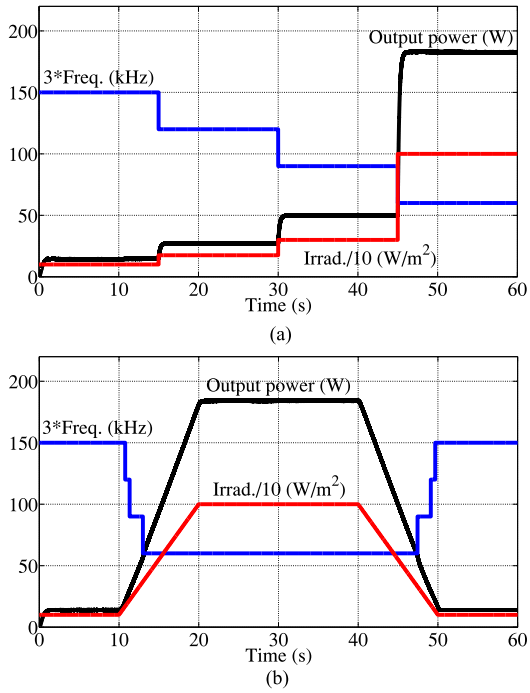

Fig. 7. Standalone case simulated irradiance, switching frequency, and power. (a) At step changing irradiance and (b) at continuously changing irradiance.

In summary, the adaptive topology and control scheme shows the expected tracking of different irradiance patterns, adjustment of the switching frequency for maintaining operation in the CCM, and efficient harvesting of the maximum available power. Meanwhile, the output voltage ripple was kept at the desired low levels by making use of both the SFM and the interleaved cell.

V. Experimental Setup and Validation

In this section, the prototyping of the MIC and the experimental setup followed by the performance results are presented. A 400-W prototype of the proposed MIC was developed. With its input and output voltage and current ratings, the prototyped MIC is suitable for most of the common PV modules and low-voltage dc microgrid standards. The MIC of a volume of 800 cm^3 and the experimental setup are shown in Fig. 8. The MIC components and the parameters of the experimental setup are listed in Table I.

A. Prototyping and Setup

1) PV Simulator: The solar array simulator *Agilent E4361A* was used to emulate the characteristics of the studied PV module at various irradiance levels through its table mode. The voltage–current characteristics of the studied module are supplied in voltage steps of 12 mV, which is the simulator's minimum voltage step.

2) Load: An electronic load in its constant resistance mode was used at the MIC output terminals for the standalone case.

3) DC Microgrid: The MIC was integrated into a dc microgrid as shown in Fig. 1. The dc-bus voltage V_o was set to 120 V. The DER of Fig. 1 was modeled by a dc power source. This DER regulates the dc-bus voltage, and the PV-MIC

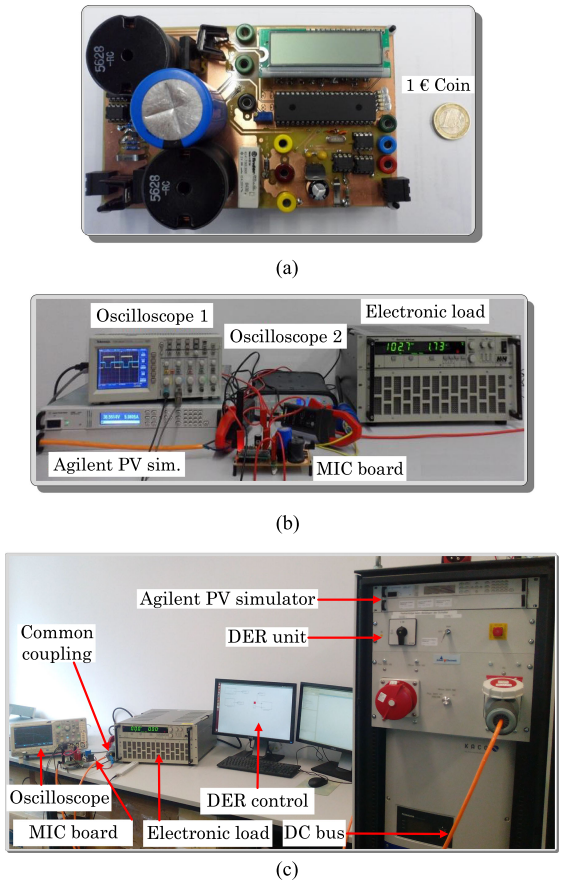

Fig. 8. (a) Module integrated converter. (b) Standalone experimental setup. (c) DC microgrid experimental setup.

TABLE I
MIC COMPONENTS AND CONTROL PARAMETERS

Component/Parameter	Value and properties
Input capacitor C_{i}	220 μF, 33 mΩ
Output capacitor C_{o}	2200 μF, 150 mΩ
Inductors $L_{1,2}$	500 μH, 85 mΩ
MOSFETs $Q_{1,2}$	150 V, 7.5 mΩ, FDP075N15A
Diodes $D_{1,2}$	180 V, 5 A, DSSK10-018A
PV module V_{oc}	44.8 V (STC)
PV module V_{MPP}	36.5 V (STC)
PV module I_{sc}	5.5 A (STC)
PV module I_{MPP}	5.1 A (STC)
Duty ratio limits $[D_{\mathrm{min}}, D_{\mathrm{max}}]$	[10 %, 90 %]
Duty ratio step ΔD	0.4 %
ADC bits and voltage	$N_{\mathrm{b}} = 10$ bit, $V_{\mathrm{ADC}} = 5$ V
Irradiance transducer gain	$A_{\mathrm{v}} = 0.005\ \mathrm{V} \cdot \mathrm{m}^2/\mathrm{W}$
Detectable irradiance change	$\Delta G_{\mathrm{min}} = 0.98\ \mathrm{W/m}^2$
Switching frequencies (kHz)	$f_{\mathrm{s0}} = 50$, $f_{\mathrm{s1}} = 40$, $f_{\mathrm{s2}} = 30$, $f_{\mathrm{s3}} = 20$
Irradiance boundaries (kW/m^2)	(0.13, 0.17), (0.18, 0.22), and (0.33, 0.37)
Interleaved converter cells	2, IBC is activated only at $f_{\mathrm{s3}} = 20$ kHz

combination acts as a current source. An electronic load of fixed resistance represents the microgrid load. Its resistance was set to 60 Ω. The dc-bus voltage, MIC output current and power, and the DER output power were recorded. The experimental setup is depicted in Fig. 8(c).

4) MIC Control for SFM and MPPT: The control algorithm was programmed on the microcontroller chip *PIC16F877A*. The microcontroller minimum duty ratio step of 0.4 % is used for accurate MPPT and for reducing the effect of limit cycle oscillation. Limit cycle oscillation results in low-frequency harmonics in the converter output voltage due to the oscillations of the duty ratio around its optimal value. The parameters of the SFM scheme are given in Table I.

Resonance issues when changing the MIC topology are avoided by deactivating the PWM signals through the MIC control for a short time interval of two sampling periods. In addition, prospective resonances are tackled by employing switching frequencies much higher than any potential resonance frequency, having damping action through the parasitic resistors, and by the implemented hysteresis effect.

5) MIC Sub-Circuits: The MIC subcircuits perform the following functions.

1) *Gate driving:* The chip *TC4427* is used for conditioning the PWM signal from the microcontroller. One of the two PWM signals in the interleaved case is subjected to a phase shift, and then, both signals are conditioned by the chip.
2) *Phase shifting:* The phase shifting of the PWM signal for the interleaved converter cell is accomplished using the chip *LTC6994-2*. According to (26) of Appendix C, five stages of the chip with single resistance R_{SET} equal to 250 kΩ are used to avoid pulse skipping and the corresponding subharmonics.
3) *Representing irradiance level:* The level of the irradiance is represented by a voltage signal from a potentiometer and is fed to the microcontroller. A physical irradiance measurement device plus a conditioning circuit may be used alternatively. For indoor laboratory testing and weather-independent environments, the approach using the potentiometer is preferred.
4) *Measuring:* The measurement of the PV module current was done with the chip *INA168* using a 20-mΩ sense resistor and a sensing gain of 40. The power loss in the sense resistor, the accuracy of measurement, and the signal conditioning for the microcontroller were the basis for determining the size of the sense resistor. The module voltage was obtained through a potential divider, a filter, and an operational amplifier *OPA340* to avoid the loading effect.

B. Performance Results

In this subsection, the system performance results are presented. This is investigated through the measurements of MIC output power, output ripple, EMI, power losses, and system efficiency. For the MIC output power and output ripple experiments, the standalone case was investigated followed by the dc microgrid case. For the EMI experiment, only the standalone case was considered to avoid EMI influence from other microgrid elements. The power losses and system efficiency were measured separately for the standalone and dc microgrid cases. Then, those measurements were averaged for result representation.

1) Output Power: The converter output power was measured for a stepwise changing irradiance. The irradiance level and the corresponding switching frequency are plotted together

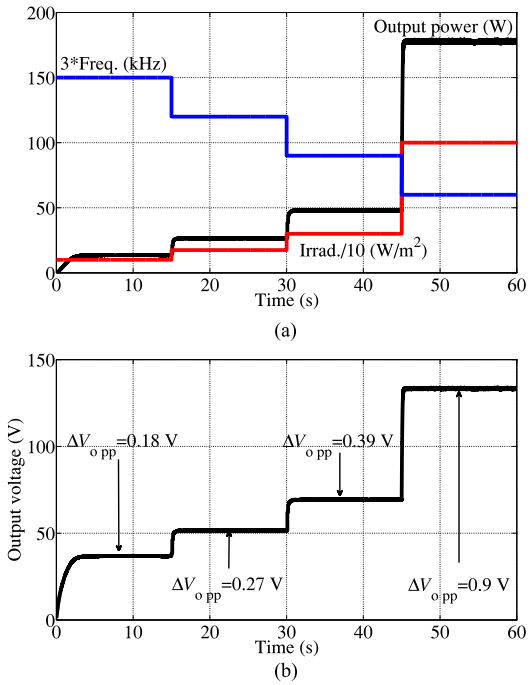

Fig. 9. Standalone case experimental step changing irradiance. (a) Output power and the switching frequency. (b) Output voltage and its ripple content.

with the module output power in Fig. 9(a) for the standalone case. The experimental results closely match the simulation results of Fig. 7(a).

For the microgrid case and under the same irradiance time series of Fig. 9(a), the dc-bus voltage and the MIC output power are depicted in Fig. 10(a). The corresponding DER output power and resistive load power are shown in Fig. 10(b). The load power of about 240 W was supplied by the PV source and DER. Therefore, the DER output power decreases with the increase of supplied PV power as a result of rising irradiance. The MIC was able to vary the switching frequency based on the irradiance, track the maximum power, and operate in the CCM.

2) Output Ripple: The output voltage and its ripple corresponding to the irradiance time series of Fig. 9(a) are shown in Fig. 9(b) for the standalone case. For the four analyzed irradiance segments, values of 0.18, 0.27, 0.39, and 0.9 V were measured for the output voltage ripple, respectively. Although the switching frequency moved from 50 to 20 kHz, the voltage ripple only increased from 0.47 % at the lowest irradiance to 0.68 % at the highest irradiance. This is thanks to the activation of the extra interleaved boost cell at 20 kHz when the irradiance is high.

The MIC output current in the dc microgrid case is shown in Fig. 10(c). The peak-to-peak output current ripple at the four irradiance segments was found to be 4, 9, 17, and 59 mA, respectively. Meanwhile, the dc-bus voltage had a ripple content of 0.3 %. As for the voltage ripple in the standalone case, the rise of the current ripple with decreasing switching frequency is also restricted through the activation of the interleaved boost cell in the dc microgrid case.

3) EMI: The radiated EMI of the highest irradiance of 1 kW/m^2 was analyzed representing the worst-case scenario

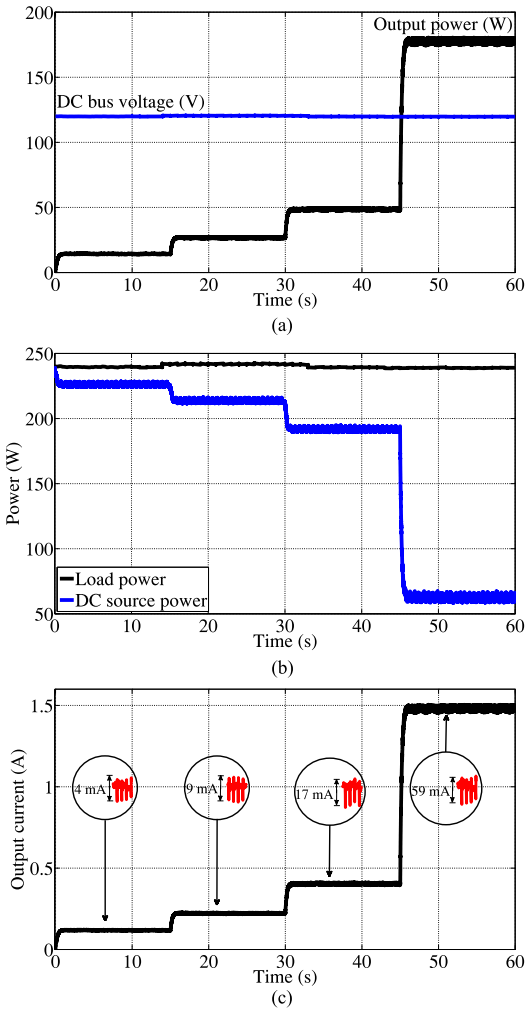

Fig. 10. DC microgrid case experimental step changing irradiance. (a) MIC output power and the dc-bus voltage. (b) Load and DER power. (c) MIC output current and its ripple content.

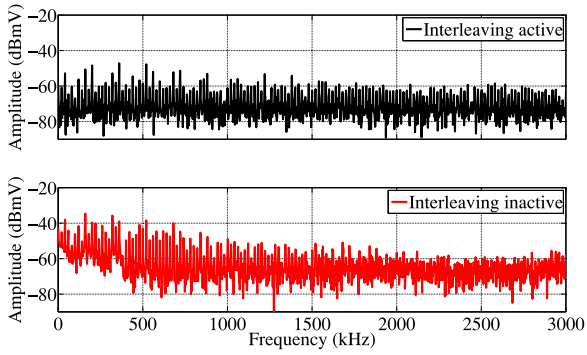

Fig. 11. MIC EMI spectrum at 1 kW/m^2 and f_s = 20 kHz with and without the interleaved MIC cell under identical operating conditions.

of highest input power. At this operating point, the SFM gives a switching frequency of 20 kHz. The results obtained for the proposed MIC are shown in the upper graph of Fig. 11. For the purpose of comparison, the interleaved cell of the MIC was then deactivated for a second experiment. The corresponding EMI spectrum is shown in the lower graph of Fig. 11. With the inter-

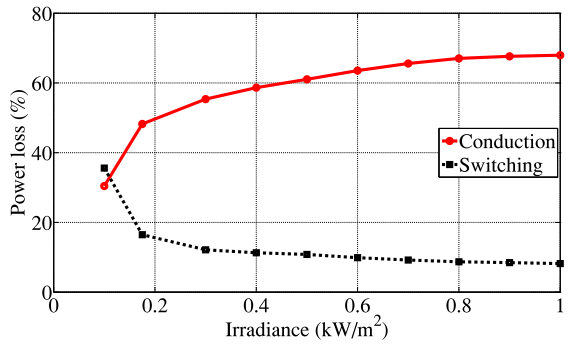

Fig. 12. MIC conduction and switching losses at different irradiance levels relative to the overall power loss.

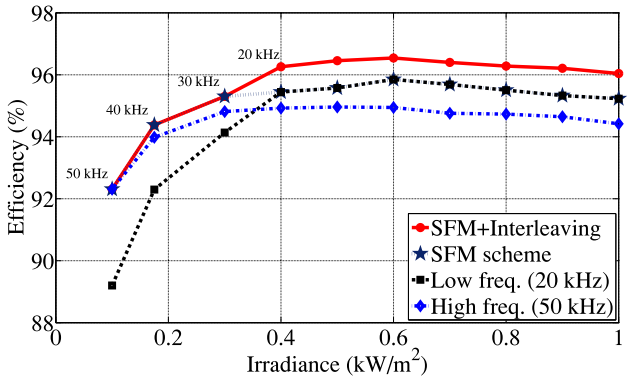

Fig. 13. Average overall efficiency at different irradiance levels for the proposed scheme in comparison to two fixed switching frequency schemes.

leaved cell active, the EMI was reduced by about 15 dB·mV. The deviation from an ideal spectrum is attributed to the continuous variation of D due to MPPT and the nonuniform phase shifting caused by delays of the switches, gate drivers, or phase-shifting circuits. The role of the interleaved converter cell in reducing EMI is consistent with the observations of [24] and [26].

4) Power Losses: The overall power losses of the MIC include the loss in tracking the MPP, the MIC conduction and switching power losses, the measurement loss, and the power needed for the control circuit. The efficiency in tracking the MPP was always above 98.5 %, keeping the MPPT losses below 1.5 % according to the readings on the *Agilent E4361A*. The power conversion efficiency was shown to be about 98 %, giving a total power conversion loss of around 2 %. The control circuit power consumption is about 1 W.

The MIC conduction and switching power losses relative to the overall power losses at different irradiances are shown in Fig. 12. At low irradiance, the switching losses are higher than conduction losses due to the high switching frequency and low PV current. At high irradiance when the PV current is high and the switching frequency is low, the contribution of the conduction losses to the total loss is much higher than for switching losses.

5) System Efficiency: The overall system efficiency at different irradiance levels was evaluated relative to other PWM schemes. The proposed adaptive SFM scheme with and without the interleaved MIC cell was compared with two fixed-frequency schemes of 50 kHz as in [3] and 20 kHz as in [6] in separate experiments. For each experiment, the steady-state MIC output power divided by the maximum trackable PV power at each irradiance level was computed. The results are shown in Fig. 13.

Compared with the fixed-high-frequency scheme, the performance of the proposed SFM scheme was similar at low irradiance. In both cases, CCM operation was maintained. At high irradiance, however, the efficiency of the proposed scheme was higher due to reduced switching losses.

The proposed SFM scheme was then compared to the fixed-low-frequency PWM scheme. At low irradiance, DCM operation was observed for the fixed-low-frequency scheme. This resulted in less harvested PV power. Therefore, less efficiency was obtained compared with the proposed SFM scheme. Only at high irradiance, the performance of the fixed low frequency and proposed SFM schemes was identical. With the activation of an interleaved MIC cell, however, an efficiency gain was to be expected. The experiment confirmed an increase of efficiency of the order of 0.5 % for this case.

For the developed control scheme, efficiencies higher than 95 % at irradiance levels above 0.175 kW/m^2 were measured. Slightly reduced efficiencies of 92.5 % and 94.3 % were found for the irradiance levels of 0.1 and 0.175 kW/m^2 due to higher switching losses. The experiments confirmed the high performance of the proposed MIC at all irradiance levels for both efficiency and power quality.

VI. Conclusion

A novel PV MIC suitable for boosting voltages for dc standalone and dc microgrid applications was designed, implemented, and tested. The proposed SFM selects an irradiance-adapted switching frequency that is always high enough to avoid operation in the DCM. At a high irradiance, the SFM sets a lower value for the frequency, guided by the strive for high efficiency through low switching losses. The proposed automated procedure has shown to be effective in searching for the optimal number and values of switching frequencies. Furthermore, an interleaved boost cell is activated at high irradiance to retain a high level of power quality. Hysteresis functions support the transitions between different discrete switching frequencies as the irradiance changes. The adaptive MIC control scheme is complemented by an MPPT designed for fast tracking. Thus, by combining the SFM with the adaptive usage of the boost converter interleaved cells and a fast MPPT, targets of efficiency and power quality are reached.

The efficiency for the entire MIC including all power conversion and control functions was measured at around 95 % or higher for irradiance levels ranging from 0.3 to 1.0 kW/m^2. The voltage ripple remained below 0.7 % during testing. The prototype was rated at 400 W to make the design well suited for integrating PV in dc microgrids or solar homes. DMPPT is implicitly supported through the module integration. The prototype's cost of parts amounted to 0.14 Euro/W when ordering parts individually in the year 2015. Scale effects will allow for further cost reductions. Together with the convincing technical performance, the cost effectiveness makes this MIC design a compelling candidate for renewable solutions of dc microgrids, dc buses, and solar home applications.

APPENDIX A
SWITCHING EFFECTS IN A BOOST CONVERTER

The average input current I_i for remaining in the CCM is $I_\mathrm{i} \geq \Delta i_\mathrm{L}/2$ and is given by [14]

$$I_\mathrm{i} \geq \frac{D \cdot V_\mathrm{i}}{2 \cdot f_\mathrm{s} \cdot L}. \tag{16}$$

The relative large MPP voltage and small MPP current at low irradiance may violate (16). Employing larger inductors can maintain the CCM. However, this entails extra cost in order not to also increase the inductor parasitic resistance

$$I_\mathrm{Lrms} = \sqrt{I_\mathrm{i}^2 + \Delta i_\mathrm{L}^2/12}. \tag{17}$$

This is used for calculating the power loss P_L in the inductor parasitic series resistance r_L. The RMS currents of the input and output capacitors are also calculated for determining the conduction losses P_Ci and P_Co in their equivalent series resistances r_Ci and r_Co, respectively [11], [34]. Then, the power loss in the MOSFET on-state resistance r_DSon, P_M, and the diode forward power loss P_D through its forward voltage drop V_fw are calculated as in [34]. Thus, the conduction power losses P_L, P_Ci, P_Co, P_M, and P_D are computed as follows:

$$P_\mathrm{L} = r_\mathrm{L} \cdot I_\mathrm{Lrms}^2 \tag{18}$$

$$P_\mathrm{Ci} = r_\mathrm{Ci} \cdot \frac{\Delta i_\mathrm{L}^2}{12} \tag{19}$$

$$P_\mathrm{Co} = r_\mathrm{Co} \cdot \left[(1-D) \cdot I_\mathrm{Lrms}^2 - I_\mathrm{o}^2\right] \tag{20}$$

$$P_\mathrm{M} = r_\mathrm{DSon} \cdot D \cdot I_\mathrm{Lrms}^2 \tag{21}$$

$$P_\mathrm{D} = V_\mathrm{fw} \cdot I_\mathrm{Lrms} \cdot (1-D). \tag{22}$$

The switching and gate losses P_SG of the MOSFET are greatly affected by the switching frequency:

$$P_\mathrm{SG} = \frac{1}{2} \cdot I_\mathrm{D} \cdot V_\mathrm{DS} \cdot f_\mathrm{s} \cdot (t_\mathrm{son} + t_\mathrm{soff}) + Q_\mathrm{g} \cdot V_\mathrm{gg} \cdot f_\mathrm{s} \tag{23}$$

where I_D is the MOSFET on-state drain current, V_DS is the MOSFET off-state drain-to-source voltage, t_son and t_soff are the MOSFET switch-on and switch-off time intervals, respectively, Q_g is the total gate charge, and V_gg is the gate driving voltage. Thus, the total power loss is computed as

$$P_\mathrm{loss} = P_\mathrm{L} + P_\mathrm{Ci} + P_\mathrm{Co} + P_\mathrm{M} + P_\mathrm{D} + P_\mathrm{SG}. \tag{24}$$

APPENDIX B
SFM SCHEME FOR A BUCK CONVERTER

The minimum switching frequency $f_\mathrm{s\,min}$ of the SFM scheme is determined by the targeted efficiency and the output voltage ripple, as in the boost converter case. The maximum switching frequency $f_\mathrm{s\,max}$ is determined as follows. The duty ratio D of the lossy buck converter is given by $D = V_\mathrm{o}/(\eta \cdot V_\mathrm{i})$ [28]. The lower limit of $f_\mathrm{s\,max}$ for the CCM is then [14]

$$f_\mathrm{s} \geq \frac{D \cdot (1-D) \cdot V_\mathrm{i}}{2 \cdot I_\mathrm{i} \cdot L}. \tag{25}$$

The expression of D is inserted in (25) with V_o as in (6), or V_o is considered constant as the bus voltage of the dc microgrid.

APPENDIX C
COST-EFFECTIVE DESIGN

Cost effectiveness has been supported by the following concepts.

1) Controller Cost-Capability Tradeoff: For the MIC, the digital control chip must have input ports for the voltage, current, and irradiance signals; one output port; three ADC channels; a PWM module; and a sufficient program memory. The microcontroller chip *PIC16F877A* fulfills these requirements, while costing less than digital signal processors (DSPs).

2) Efficient Utilization of Low-Cost Current Measurement Chips: The often limited accuracy of low-cost current measurement chips can be overcome through appropriate MPPT algorithms. The P&O MPPT algorithm compares the most recent and previous module power and voltage for tracking the MPP. When small perturbation steps are employed, the currents of the adjacent perturbation steps are close to each other. Thus, the deterministic measurement errors are reduced. MPPT algorithms that require more accurate measurements would entail a higher chip cost.

3) Effective Diode Configuration: Employing the two parallel diodes of low-cost chips reduces the power loss based on the nonlinear relation between power loss and the flowing current.

4) Facile Phase Shifting: A variable delay chip was used with a delay time T_d of half the used switching period, $0.5/f_\mathrm{s3}$, implementing a phase shifting of 180°. Delaying fast successive edges of the PWM signal can lead to pulse skipping in the PWM signal and subharmonics in the converter output. Therefore, the delay time must be less than the minimum on-time of the PWM signal, $T_\mathrm{ONmin} = D_\mathrm{min}/f_\mathrm{s3}$, or the delay time will have to be divided equally between multiple stages. The number of delaying stages N_d is determined from

$$N_\mathrm{d} = \frac{T_\mathrm{d}}{T_\mathrm{ONmin}}. \tag{26}$$

ACKNOWLEDGMENT

The authors would like to gratefully acknowledge the assistance of Kerstin Trubel in developing the MIC prototype.

REFERENCES

[1] REN21. 2016, "Renewables 2016 global status report," Renewable Energy Policy Network for the 21st Century, Paris, France, Tech. Rep. 4564, 2016.
[2] E. Romero-Cadaval, G. Spagnuolo, L. G. Franquelo, C. A. Ramos-Paja, T. Suntio, and W. M. Xiao, "Grid-connected photovoltaic generation plants: Components and operation," *IEEE Ind. Electron. Mag.*, vol. 7, no. 3, pp. 6–20, Sep. 2013.
[3] M. Das and V. Agarwal, "Design and analysis of a high-efficiency DC-DC converter with soft switching capability for renewable energy applications requiring high voltage gain," *IEEE Trans. Ind. Electron.*, vol. 63, no. 5, pp. 2936–2944, May 2016.
[4] F. Wang, F. Zhuo, F. C. Lee, T. Zhu, and H. Yi, "Analysis of existence-judging criteria for optimal power regions in DMPPT PV systems," *IEEE Trans. Energy Convers.*, vol. 31, no. 4, pp. 1433–1441, Dec. 2016.
[5] O. Khan, W. Xiao, and M. S. E. Moursi, "A new PV system configuration based on submodule integrated converters," *IEEE Trans. Power Electron.*, vol. 32, no. 5, pp. 3278–3284, May 2017.
[6] F. Wang, T. Zhu, F. Zhuo, H. Yi, S. Shi, and X. Zhang, "Analysis and optimization of flexible MCPT strategy in submodule PV application," *IEEE Trans. Sustain. Energy*, vol. 8, no. 1, pp. 249–257, Jan. 2017.

[7] M. A. G. de Brito, L. Galotto, L. P. Sampaio, G. d. A. e Melo, and C. A. Canesin, "Evaluation of the main MPPT techniques for photovoltaic applications," *IEEE Trans. Ind. Electron.*, vol. 60, no. 3, pp. 1156–1167, Mar. 2013.
[8] F. F. Edwin, W. Xiao, and V. Khadkikar, "Dynamic modeling and control of interleaved flyback module-integrated converter for PV power applications," *IEEE Trans. Ind. Electron.*, vol. 61, no. 3, pp. 1377–1388, Mar. 2014.
[9] A. M. S. S. Andrade, L. Schuch, and M. L. da Silva Martins, "High step-up PV module integrated converter for PV energy harvest in FREEDM systems," *IEEE Trans. Ind. Appl.*, vol. 53, no. 2, pp. 1138–1148, Mar. 2017.
[10] C. T. Pan, M. C. Cheng, C. M. Lai, and P. Y. Chen, "Current-ripple-free module integrated converter with more precise maximum power tracking control for PV energy harvesting," *IEEE Trans. Ind. Appl.*, vol. 51, no. 1, pp. 271–278, Jan. 2015.
[11] M. Adly and K. Strunz, "Switching frequency optimized granular maximum power point tracking for PV systems," in *Proc. IEEE PES Innovative Smart Grid Technol. Conf. Eur.*, Istanbul, Turkey, Oct. 2014, pp. 1–7.
[12] B. W.-K. Ling, C. Bingham, H. H.-C. Iu, and K.-L. Teo, "Combined optimal pulse width modulation and pulse frequency modulation strategy for controlling switched mode DC-DC converters over a wide range of loads," *IET Control Theory Appl.*, vol. 6, no. 13, pp. 1973–1983, Sep. 2012.
[13] C. A. Yeh, and Y. S. Lai, "Digital pulsewidth modulation technique for a synchronous buck DC/DC converter to reduce switching frequency," *IEEE Trans. Ind. Electron.*, vol. 59, no. 1, pp. 550–561, Jan. 2012.
[14] N. Mohan, T. M. Undeland, and W. P. Robbins, *Power Electronics: Converters, Applications and Design*, 3rd ed. New York, NY, USA: Wiley, 2003.
[15] O. Oederra, I. Kortabarria, I. M. de Alegra, J. Andreu, and J. I. Grate, "Three-phase VSI optimal switching loss reduction using variable switching frequency," *IEEE Trans. Power Electron.*, vol. 32, no. 8, pp. 6570–6576, Aug. 2017.
[16] T. Konjedic, L. Koroec, M. Trunti, C. Restrepo, M. Rodi, and M. Milanovi, "DCM-based zero-voltage switching control of a bidirectional DC-DC converter with variable switching frequency," *IEEE Trans. Power Electron.*, vol. 31, no. 4, pp. 3273–3288, Apr. 2016.
[17] W. Al-Hoor, J. A. Abu-Qahouq, L. Huang, W. B. Mikhael, and I. Batarseh, "Adaptive digital controller and design considerations for a variable switching frequency voltage regulator," *IEEE Trans. Power Electron.*, vol. 24, no. 11, pp. 2589–2602, Nov. 2009.
[18] K. K. Tse, R. W.-M. Ng, H. S.-H. Chung, and S. Y. R. Hui, "An evaluation of the spectral characteristics of switching converters with chaotic carrier-frequency modulation," *IEEE Trans. Ind. Electron.*, vol. 50, no. 1, pp. 171–182, Feb. 2003.
[19] Z. Yang, H. Li, Z. Li, and W. A. Halang, "Spectrum calculation method for a boost converter with chaotic PWM," in *Proc. 18th Eur. Conf. Power Electron. Appl.*, Sep. 2016, pp. 1–6.
[20] W. R. Liou, H. M. Villaruza, M. L. Yeh, and P. Roblin, "A digitally controlled low-EMI SPWM generation method for inverter applications," *IEEE Trans. Ind. Informat.*, vol. 10, no. 1, pp. 73–83, Feb. 2014.
[21] H. J. Choi and J. H. Jung, "Enhanced power line communication strategy for DC microgrids using switching frequency modulation of power converters," *IEEE Trans. Power Electron.*, vol. 32, no. 6, pp. 4140–4144, Jun. 2017.
[22] K. Gnanasambandam, A. Edpuganti, A. K. Rathore, D. Srinivasan, C. Cecati, and C. Buccella, "Optimal low switching frequency pulsewidth modulation of current-fed three-level converter for solar power integration," *IEEE Trans. Ind. Electron.*, vol. 63, no. 11, pp. 6877–6886, Nov. 2016.
[23] M. M. Ghahderijani, M. Castilla, A. Momeneh, J. T. Miret, and L. G. de Vicuna, "Frequency-modulation control of a DC/DC current-source parallel-resonant converter," *IEEE Trans. Ind. Electron.*, vol. 64, no. 7, pp. 5392–5402, Jul. 2017.
[24] S. Kimura, Y. Itoh, W. Martinez, M. Yamamoto, and J. Imaoka, "Downsizing effects of integrated magnetic components in high power density DC-DC converters for EV and HEV applications," *IEEE Trans. Ind. Appl.*, vol. 52, no. 4, pp. 3294–3305, Jul. 2016.
[25] S. Prabhakar and F. Daya, "A comparative study on the performance of interleaved converters for EV battery charging," in *Proc. IEEE 6th Int. Conf. Power Syst.*, Mar. 2016, pp. 1–6.
[26] P. Zumel, O. Garcia, J. A. Oliver, and J. A. Cobos, "Differential-mode EMI reduction in a multiphase DCM flyback converter," *IEEE Trans. Power Electron.*, vol. 24, no. 8, pp. 2013–2020, Aug. 2009.
[27] K. Mainali and R. Oruganti, "Conducted EMI mitigation techniques for switch-mode power converters: A survey," *IEEE Trans. Power Electron.*, vol. 25, no. 9, pp. 2344–2356, Sep. 2010.
[28] M. K. Kazimierczuk, *Pulse-width Modulated DC-DC Power Converters*. Chichester, U.K.: Wiley, 2008.
[29] D. Salomonsson and A. Sannino, "Low-voltage DC distribution system for commercial power systems with sensitive electronic loads," *IEEE Trans. Power Del.*, vol. 22, no. 3, pp. 1620–1627, Jul. 2007.
[30] Y. Qiu, L. Wang, H. Wang, Y. F. Liu, and P. C. Sen, "Bipolar ripple cancellation method to achieve single-stage electrolytic-capacitor-less high-power LED driver," *IEEE J. Emerg. Sel. Topics Power Electron.*, vol. 3, no. 3, pp. 698–713, Sep. 2015.
[31] M. Adly, M. Ibrahim, and H. El Sherif, "Comparative study of improved energy generation maximization techniques for photovoltaic systems," in *Proc. Asia-Pacific Power Energy Eng. Conf.*, Shanghai, China, Mar. 2012, pp. 1–5.
[32] D. Wu, F. Tang, T. Dragicevic, J. M. Guerrero, and J. C. Vasquez, "Coordinated control based on bus-signaling and virtual inertia for islanded DC microgrids," *IEEE Trans. Smart Grid*, vol. 6, no. 6, pp. 2627–2638, Nov. 2015.
[33] K. Strunz, E. Abbasi, and D. N. Huu, "DC microgrid for wind and solar power integration," *IEEE J. Emerg. Sel. Topics Power Electron.*, vol. 2, no. 1, pp. 115–126, Mar. 2014.
[34] G. R. Walker and P. C. Sernia, "Cascaded DC-DC converter connection of photovoltaic modules," *IEEE Trans. Power Electron.*, vol. 19, no. 4, pp. 1130–1139, Jul. 2004.

Moustafa Adly (S'14) received the B.Sc.(Hons.) degree in electronics and electrical communications from Cairo University, Cairo, Egypt, in 2004 and the M.Sc. degree in electronics and electrical energy systems with A^+ from the German University in Cairo, in 2011. He has been working toward the Ph.D. degree with Technische Universität Berlin, Berlin, Germany, since April 2013.

He has worked with Cairo University and the German University in Cairo as a Researcher and Lecturer Assistant. He is a Research Scientist and Lecturer with Technische Universität Berlin. He is a reviewer for several international journals including IEEE TRANSACTIONS. His research interests include photovoltaics, power electronics, control systems, and dc microgrids.

Kai Strunz received the Dipl.-Ing. and Dr.-Ing. (*summa cum laude*) degrees from Saarland University, Saarbrücken, Germany, in 1996 and 2001, respectively.

From 1995 to 1997, he pursued research with Brunel University, London, U.K. From 1997 to 2002, he worked with the Division Recherche et Développement of Electricité de France in the Paris area. From 2002 to 2007, he was an Assistant Professor of electrical engineering with the University of Washington, Seattle, WA, USA. Since September 2007, he has been a Professor for sustainable electric networks and sources of energy with Technische Universität Berlin, Berlin, Germany.

Dr. Strunz is the Chairman of the IEEE Power and Energy Society (PES) Subcommittee on Distributed Energy Resources. He received the IEEE PES Prize Paper Award in 2015 and the IEEE JOURNAL OF EMERGING AND SELECTED TOPICS IN POWER ELECTRONICS First Prize Paper Award in 2015. He was the Chairman of the conference IEEE PES Innovative Smart Grid Technologies held at Technische Universität Berlin, October 14–17, 2012. On behalf of the Intergovernmental Panel on Climate Change, he was a Review Editor for the Special Report on Renewable Energy Sources and Climate Change Mitigation.